Inertia–Gravity Waves Observed in the Lower Stratosphere over Macquarie Island

FIONA M. GUEST

Cooperative Research Centre for Southern Hemisphere Meteorology, Monash University, Clayton, Victoria, Australia

MICHAEL J. REEDER

Department of Mathematics and Statistics, Monash University, Clayton, Victoria, Australia

CRISPIN J. MARKS

National Institute for Water and Atmosphere Research, Hamilton, New Zealand

DAVID J. KAROLY

Cooperative Research Centre for Southern Hemisphere Meteorology, Monash University, Clayton, Victoria, Australia

(Manuscript received 3 June 1998, in final form 26 April 1999)

ABSTRACT

This study examines the properties of inertia–gravity waves observed in the lower stratosphere over Macquarie Island, how these properties vary with season, and the likely source of the waves. The waves are observed in high-resolution upper-air ozonesonde soundings of wind and temperature released from Macquarie Island during the 1994 ASHOE–MAESA program.

The properties of the inertia–gravity waves observed in the soundings are quantified using hodograph and rotary spectral analyses. The analyzed waves have horizontal wavelengths between 100 and 1000 km, vertical wavelengths between about 1 and 7 km, intrinsic frequencies between f and $2f$, and horizontal trace speeds between -50 and 30 m s^{-1}. There appears to be a seasonal cycle in the inertia–gravity wave activity in the lower stratosphere, the minimum being in the austral winter when the background zonal flow is strong and westerly and its vertical shear is positive. In contrast, the variance of the horizontal perturbation winds does not show a similar seasonal cycle.

Inertia–gravity waves are detected over Macquarie Island on days with a common synoptic pattern. Two features define this synoptic pattern: 1) an upper-level jet and associated surface front lying upstream of Macquarie Island, and 2) a 300-hPa height field with Macquarie Island located between the inflection axis and the downstream ridge. This common synoptic pattern is observed on 16 of the 21 days on which inertia–gravity waves were detected. Moreover, the pattern is not observed on 15 of the 21 days in which inertia–gravity waves are not identified. This common synoptic pattern shows a seasonal cycle similar to that found for the inertia–gravity wave activity. Analyses of the ozonesonde soundings suggest also that the source of the inertia–gravity waves is in the troposphere. Using GROGRAT, the ray-tracing model developed by Marks and Eckermann, a cone of rays is released 21 km above Macquarie Island and traced backward in time. These rays suggest that the inertia–gravity waves are generated in the jet–front system southwest of Macquarie Island.

1. Introduction

It is thought that the internal gravity waves commonly observed in the middle atmosphere are generated mostly in the troposphere by flow over orography, by convection and by jet–front systems (see, e.g., Fritts 1993, and references therein). Those gravity waves that radiate upward from the troposphere into the middle atmosphere have an associated vertical flux of horizontal momentum. When such waves are transient or suffer attenuation by any means (e.g., saturation, wave breaking, or diffusion), horizontal momentum is transferred to the mean flow, and such a transfer may be interpreted as a force on the mean flow. Thus, even though the waves are generated in the troposphere, they may apply a stress far from their source region. In this way upward-radiating internal gravity waves couple the troposphere to the atmosphere above by redistributing momentum

Corresponding author address: Fiona Guest, Cooperative Research Centre for Southern Hemisphere Meteorology, Monash University, Wellington Rd., Clayton, Victoria 3168, Australia.
E-mail: fiona@vortex.shm.monash.edu.au

and energy, and play an important part in shaping the general circulation of the middle atmosphere.

Recently, Allen and Vincent (1995) examined the properties of gravity waves in the lower stratosphere using high-resolution measurements of temperature and pressure made by radiosondes released operationally by the Australian Bureau of Meteorology. They constructed a climatology of wave energy over Australia and the Southern Ocean and showed, among other things, that the wave activity was highest in the Tropics. Following this, Vincent et al. (1997) examined the properties of gravity waves in the lower stratosphere using Omega-sonde observations taken at Macquarie Island (54°S, 159°E) from 1993 to 1994. The advantage that Omega-sondes have over conventional radiosondes is that they provide high-resolution observations of wind as well as the usual temperature and pressure measurements. Vincent et al. showed that the wave energy is largest near the inertial frequency and that the waves seem to have preferential directions of propagation, especially during winter.

The central aims of the present study are to examine the properties of inertia–gravity waves (gravity waves with intrinsic frequencies close to the inertial frequency) in the Southern Hemisphere lower stratosphere, and to investigate the likely source of the waves. Like Vincent et al. (1997), the study presented here is based on Omega-sondes released from Macquarie Island. However, unlike Vincent et al., our study uses sondes that measured ozone also, and consequently reached substantially higher heights in the stratosphere than the conventional Omega-sondes analyzed by Vincent et al. Thus, our study complements and extends their work.

Since the mean density of the atmosphere decreases with height, the amplitude of upward-propagating gravity waves increase with height. For this reason, gravity waves are generally more easily detected in the stratosphere than in the troposphere. Moreover, gravity waves in the troposphere can be masked by large perturbations in the wind and temperature associated with weather systems (such as fronts and extratropical cyclones) and convection. Therefore, our gravity wave analysis focuses on the stratosphere.

The remainder of the paper is set out as follows. Section 2 describes the Omega-sonde soundings that form the basis of our inertia–gravity wave analysis. These soundings are decomposed into a background flow and a perturbation that we identify as the gravity wave. The decomposition method is also described briefly in section 2. In section 3 we present a simple hodograph analysis. Section 4 describes a rotary spectral analysis of the gravity wave profiles. Following this, the wave properties are deduced using linear gravity wave theory and the results are discussed in section 5. The seasonal variability of the wave activity and the wave parameters is also examined. In section 6 synoptic weather analyses and ray-tracing calculations are combined to investigate the source of the waves. Our summary and conclusions are set out in section 7.

2. Sounding data

Much of the following analysis is based on high-resolution upper-air Omega-sonde ozone soundings launched approximately weekly from Macquarie Island as part of the 1994 Airborne Southern Hemisphere Ozone Experiment–Measurements for Assessing the Effects of Stratospheric Aircraft (ASHOE–MAESA) program. A total of 47 soundings were made, of which 42 reached heights of 30 km or more. Since this paper focuses on the lower stratosphere, only those soundings that reached 30 km are used in the analysis. The soundings measured pressure, temperature, relative humidity, dewpoint temperature, and horizontal wind direction and wind speed every 10 s (or roughly every 50 m in the vertical). Between 3 and 1060 hPa, the pressure sensor on the Omega-sonde has a resolution of ± 0.1 hPa and an accuracy of ± 0.5 hPa. The temperature has a resolution of ± 0.1 K and is accurate to ± 0.2 K over the interval 183–333 K. The humidity sensor has a resolution of $\pm 1.0\%$ RH and is accurate to $\pm 2.0\%$ RH. Finally, the random error in each component of the wind is approximately 0.5 m s^{-1}. Figure 1 summarizes the data, showing the date of each sounding and the height of each sounding (triangles). The tropopause height (circle) is plotted also and lies between 8 and 12 km above ground level.

Individual soundings are separated into background and perturbation profiles, and the perturbation profiles are analyzed for inertia–gravity waves. Using the method of least squares, fourth-order polynomials are fitted to each wind and temperature sounding over the intervals 0–9 km and 12–30 km (see section 5b for further discussion on this choice). These polynomials define the background profiles, and the differences between the soundings and the background profiles define the wave fields. For example, Fig. 2 shows the zonal and meridional wind, and temperature soundings between 12 and 30 km on 25 October 1994, together with the corresponding background and perturbation profiles. Using a Fourier transform, the perturbations profiles are filtered to remove the very low- and very high-frequency oscillations; the details of the filter are explained in section 4. To reduce leakage, a 1.5-km segment at each end of the data is tapered using the Hanning window. Only filtered data are used in the following analyses, and mostly the analysis is confined to the height interval between 13.5 and 28.5 km.

3. Hodograph analysis

Consider a monochromatic inertia–gravity wave propagating in a uniform background flow. In a frame of reference moving with the background flow, the wave's hodograph traces out an ellipse. The ratio of the

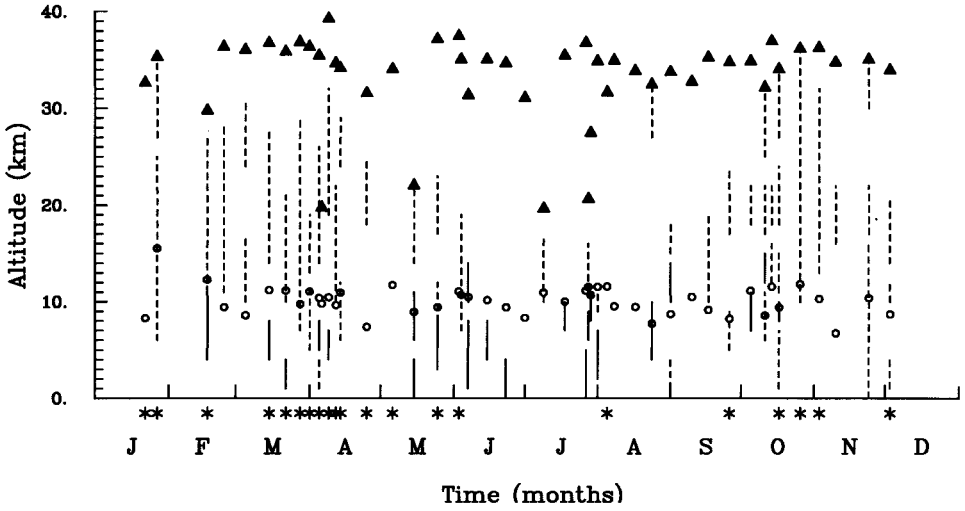

FIG. 1. Summary of the 47 ozonesonde flights. The maximum height reached is marked by the triangles and the circles show the tropopause height. Dashed lines mark those regions showing clear evidence of anticyclonic rotation in the hodographs. Similarly, the solid lines mark regions of cyclonic rotation. Asterisks mark the flights that passed the gravity wave test.

semiminor and semimajor axes, the eccentricity, is proportional to the ratio of the local value of the Coriolis parameter f and the intrinsic frequency ω_*. The intrinsic frequency is the frequency of the wave as measured by an observer moving with the background flow. The orientation of the major axis of the ellipse gives the horizontal direction in which the wave propagates ($\pm 180°$). Upward-propagating waves have hodographs that rotate anticyclonically with time, while conversely downward-propagating waves are characterized by cyclonically rotating hodographs. [See, e.g., Gill (1982) for a more detailed discussion of inertia–gravity waves and their properties.]

The ideal inertia–gravity wave described above has been used in many studies as the basis for identifying inertia–gravity waves in soundings. (See, e.g., Hirota and Niki 1985; Tsuda et al. 1994; Sato 1994; Karoly et al. 1996.) Figure 3 shows the hodograph of the perturbation winds (14–34 km) on 25 October 1994 (the same sounding used in Fig. 2) and is typical of most of the soundings taken. In this figure the abscissa measures the zonal perturbation wind component u', while the meridional perturbation wind component v' is plotted against the ordinate. The crosses mark the height of the balloon above ground level at 1-km intervals. The perturbation wind vector makes about four complete counterclockwise (i.e., anticyclonic in the Southern Hemisphere) rotations, implying upward energy propagation. Figure 1 summarizes the hodographs from all the soundings. The dashed vertical lines mark the regions of anticyclonic rotation and the solid lines mark similar regions of cyclonic rotation. This figure shows that anticyclonic rotation (i.e., upward energy propagation) is dominant in the stratosphere, and that cyclonic rotation (i.e., downward energy propagation) is more common in the troposphere. Taken together these results suggest that the source region for the waves is probably in the troposphere. At times the hodographs show clear rotation through most of the sounding, although there appears to be a lack of clear rotation above the tropopause in the austral winter months (i.e., June, July, and August).

There are, of course, severe limitations in applying the hodograph method. First, the method assumes linear monochromatic waves. Second, only the relatively low-frequency inertia–gravity waves can be detected using this method because at higher frequencies the ellipse collapses to a line. In other words, the waves are linearly polarized. It is important to bear these limitations in mind when interpreting the observations. For example, it is not possible to tell whether the relative minimum in anticyclonic rotation in the stratosphere observed during winter (Fig. 1) reflects a genuine reduction in wave activity since higher-frequency waves are undetectable.

4. Spectral analysis

This section describes a spectral analysis of the sounding data. As the method used here to identify the inertia–gravity wave signal in the Omega-sonde soundings is a little different from the methods used by previous investigators (e.g., Vincent 1984; Barat and Cot 1992), it is appropriate to briefly summarize our approach.

a. Apparent frequency spectra

The key difference between our approach to spectral analysis and the approach taken by others is that we treat the soundings as time series (instead of instanta-

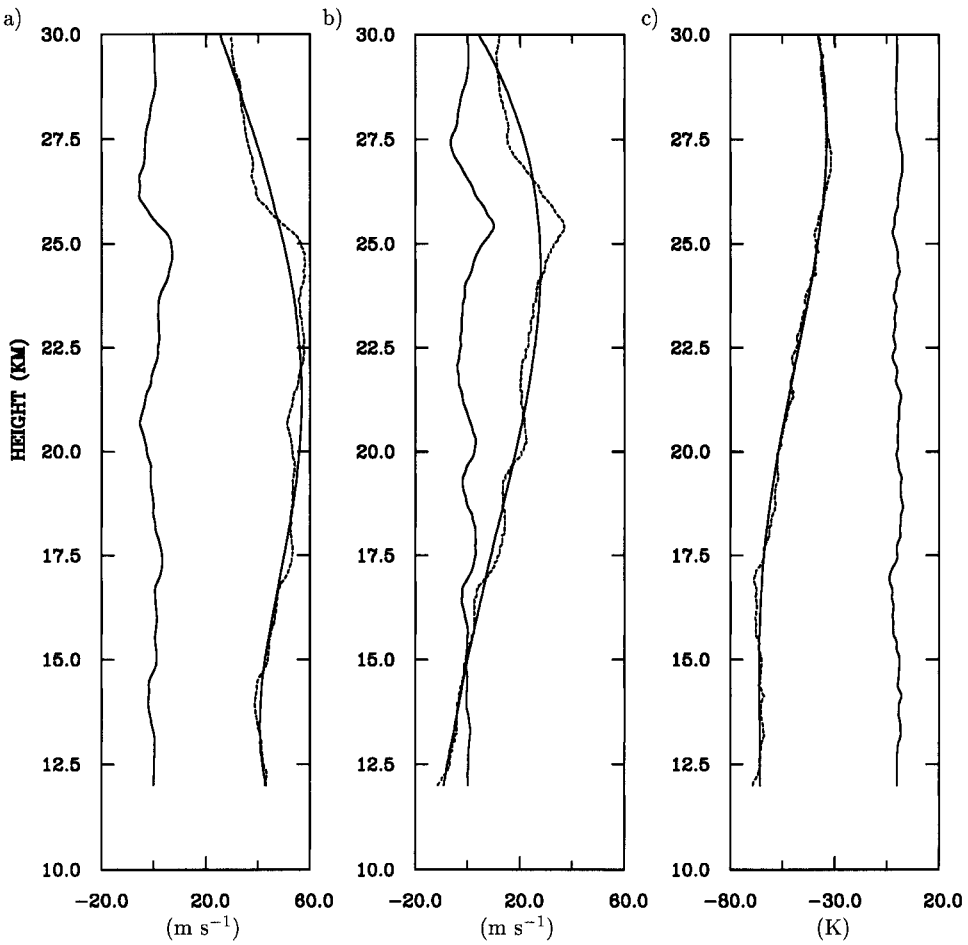

FIG. 2. (a) Vertical profiles of the zonal wind u (dashed line), the perturbation zonal wind u' (solid line centered at 0 m s^{-1}), and the background zonal wind defined by a fourth-order polynomial least squares fit to u (solid curve overlaying u). The sounding was made on 25 Oct 1994. (b) As for (a) except for meridional wind; (c) as for (a) except for temperature.

neous height profiles) and analyze the data in a frame of reference moving with the balloon. The advantage of this method is that the analysis takes into account the Doppler shifting of the wave field by the balloon as well as the Doppler shifting by the background wind.

Consider a single plane wave with phase

$$\alpha = kx + ly + mz - \omega t, \tag{1}$$

where k and l are the horizontal components of the wavenumber vector in the x and y directions, respectively; m is the vertical wavenumber; z is the height coordinate; ω is the ground-based frequency; and t is the time. The Omega-sonde follows a trajectory described by

$$[x(t), y(t), z(t)] = (x_0, y_0, z_0) + \int_0^t [u(t), v(t), w(t)]\, dt$$

$$\approx (x_0, y_0, z_0) + \int_0^t [U, V, W_b]\, dt, \tag{2}$$

where (x_0, y_0, z_0) is the initial position of the Omega-sonde, (u, v, w) is the velocity, (U, V) is the horizontal background wind, and W_b is the vertical velocity of the balloon.

Combining Eqs. (1) and (2), the phase of the wave can be rewritten as

$$\alpha - \alpha_0 = -(\omega - kU - lV - mW_b)t$$

$$= -(\omega_* - mW_b)t = -\Omega t, \tag{3}$$

where $\alpha_0 = kx_0 + ly_0 + mz_0$ is the initial phase. Here Ω is called the apparent frequency, that being the frequency of the wave as measured by an observer moving with the Omega-sonde. Equation (3) implies that if the Omega-sonde sounding is treated as a time series, then the Fourier transform of a sounding gives the apparent frequency.

We examine now the conditions under which Omega-sonde soundings can be treated as instantaneous height profiles. From Eq. (3), the change in phase measured by the Omega-sonde will be dominated by changes in

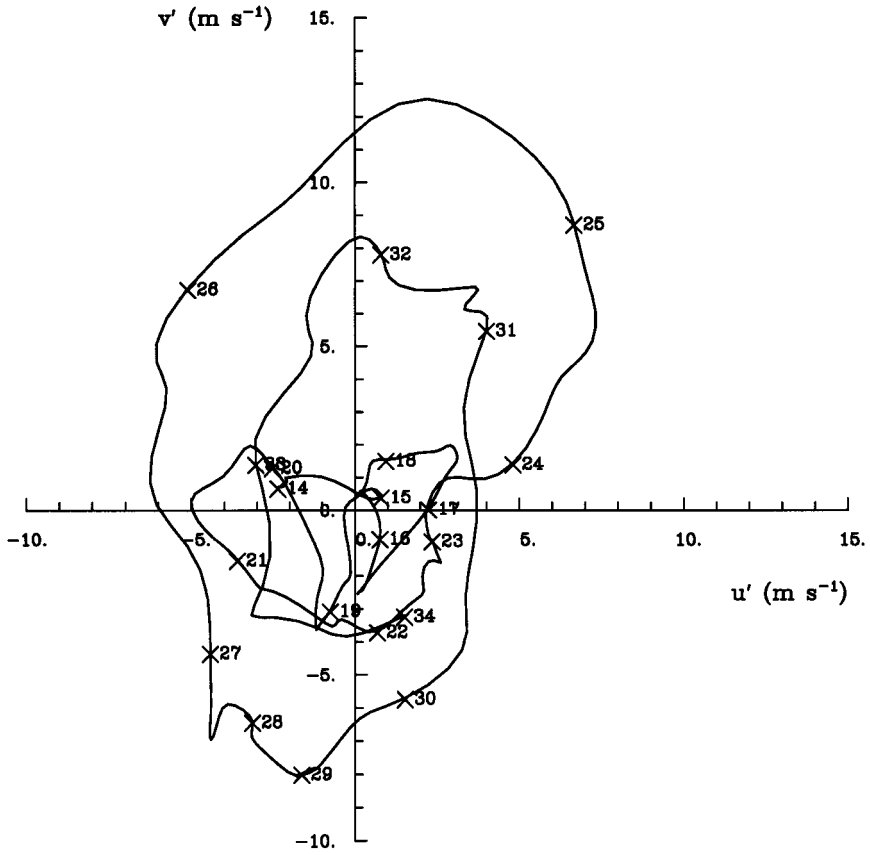

FIG. 3. Typical hodograph of the horizontal perturbation wind. This sounding was made on 25 Oct 1994. The horizontal axis marks the perturbation zonal wind component u' and the vertical axis the perturbation meridional wind component v'. The height (in km) is shown at each cross (x) and the winds have units of m s^{-1}.

the vertical when $\omega_* \ll mW_b$. In this case, the sounding made by the Omega-sonde is approximately an instantaneous vertical profile. This condition may be re-expressed as

$$\gamma = \left| \frac{\lambda_z}{\tau_* W_b} \right| \ll 1, \tag{4}$$

where $\tau_* = 2\pi/(\omega_*)$ is the intrinsic period and $\lambda_z = 2\pi/m$ is the vertical wavelength.

In practice, it makes little difference to the results whether the soundings are treated as time series or whether they are treated as instantaneous height profiles (see section 5b). This is because γ is generally much smaller than unity for inertia–gravity waves. For example, typical values for the parameters in Eq. (4) are $W_b \approx 5$ m s^{-1}, $\lambda_z \approx 3 \times 10^3$ m, and $\tau_* \approx 3 \times 10^4$ s, giving $\gamma \approx 0.02$. One of the chief advantages of the time-series method is that it helps clarify the limitations in using radiosondes to study inertia–gravity waves.

As mentioned in section 2, the perturbation wind and temperature fields are bandpass filtered to remove very low- and very high-frequency oscillations. Peaks in the temperature power spectrum were found to lie within the interval 0.001–0.1 rad s^{-1}. Therefore, to help isolate the gravity wave signal, oscillations with apparent frequencies outside this interval were removed.

b. Wave activity

We consider now a rotary spectral analysis of the perturbation wind fields. The technique quantifies how energy is partitioned between upward- and downward-propagating inertia-gravity waves. The rotary spectrum is derived from the power spectrum of $u'(t) + iv'(t)$, where $i = \sqrt{-1}$, and $u'(t)$ and $v'(t)$ are time series of the perturbation velocities (following the balloon). The clockwise (counterclockwise) rotating waves are associated with positive (negative) frequencies in the rotary power spectrum. For further details on rotary spectra, see Leaman and Sanford (1975) and Gonella (1972).

Figure 4 shows the energy-preserving form of rotary spectrum (i.e., the product of the power and Ω is plotted on the ordinate) for 25 October 1994. The analysis is confined to the height range 13.5–28.5 km. The dashed line in Fig. 4 represents the counterclockwise part (anticyclonic in the Southern Hemisphere) and the solid

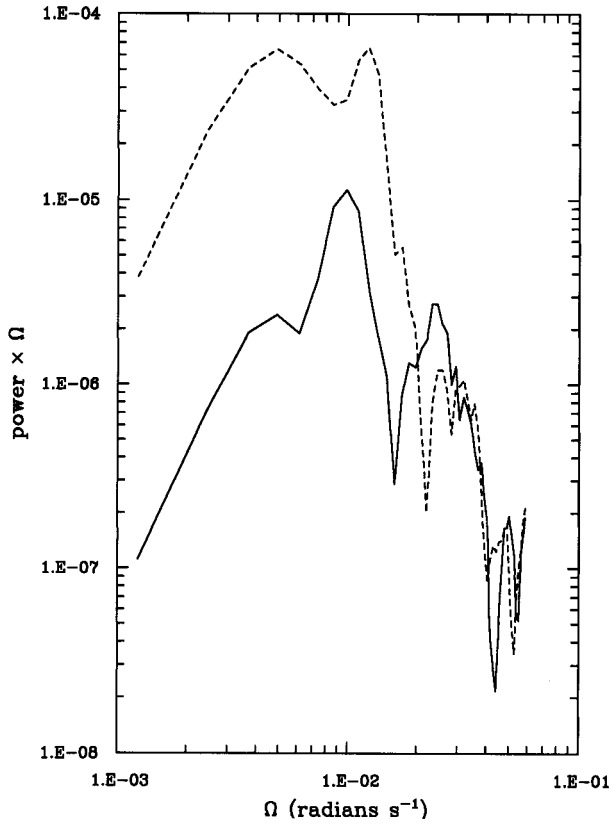

FIG. 4. Three-point averaged energy-preserving rotary spectrum for 25 Oct 1994; the cyclonic component is shown by the solid line and the anticyclonic component by the dashed line.

line represents the clockwise part (cyclonic in the Southern Hemisphere). Not surprisingly, most of the energy is associated with the anticyclonic part of this rotary spectrum. The slope of the spectrum is approximately -2.4, which is typical of vertical wavenumber spectra (see Bacmeister et al. 1996). One expects the vertical wavenumber spectrum to be very similar to the apparent frequency spectrum since $\gamma \ll 1$.

The partition of energy between upward- and downward-propagating waves can be characterized by the rotary power ratio $\mathcal{R}$, which we define by

$$\mathcal{R} = \frac{\int \Omega P_{AC}\, d\Omega}{\int (\Omega P_{AC} + \Omega P_C)\, d\Omega}. \tag{5}$$

Here P_{AC} refers to the counterclockwise part of the *energy-preserving* rotary spectrum and P_C refers to the clockwise part. For purely counterclockwise rotation, $\mathcal{R} = 1$; for purely clockwise rotation, $\mathcal{R} = 0$; and $\mathcal{R} \approx 0.5$ for linearly polarized waves, noise, or when upward- and downward-propagating inertia–gravity waves make equal contributions to the spectrum. For example, $\mathcal{R} = 0.88$ on 25 October 1994 (Fig. 4).

Figure 5 shows $\mathcal{R}$ for the 42 soundings that reach at least 30 km. Values of $\mathcal{R}$ between the solid lines are probably not sufficiently different from 0.5 to indicate a significant bias toward upward or downward inertia-gravity wave propagation. Here $\mathcal{R}$ is calculated in the stratosphere between 13.5 and 28.5 km, and in the troposphere between 1 and 8 km. As in Fig. 1, there is little evidence for upward-propagating inertia–gravity waves above the tropopause during the austral winter. This may reflect a shift in the wave activity from lower to higher frequencies, or, as argued later in section 6a, it may reflect a real seasonal variation in inertia–gravity wave activity. Note, however, that the analysis is ambiguous if the source lies within the analysis height interval. Nevertheless, as seen in Fig. 1, cyclonic rotations were rarely observed within the stratosphere, suggesting that the source region lay in the troposphere. Upward-propagating waves appear to be prominent in the stratosphere during the remainder of the year. In the troposphere, clockwise rotations are more common. Therefore, the source region for the waves is probably in the troposphere, as mentioned earlier.

The variance $(\overline{u'^2 + v'^2})$ is commonly used as a measure of gravity wave activity. A time series of the variance constructed from all 42 soundings (13.5–28.5 km) is shown in Fig. 6. Using the methods discussed in section 5a, the estimated errors in the variance are less than 3%. The variance does not show any clear seasonal variation and appears to bear little relation to results from the hodograph and rotary spectra analyses. If upward- and downward-propagating waves were present, or if the wave frequencies were large compared to f, the data would show large variance even though $\mathcal{R}$ would be close to 0.5. In contrast to these results, Eckermann et al. (1995) report a seasonal cycle in the variance with a peak during winter and a minimum during summer.

5. Wave parameters

In this section, important wave parameters are estimated from the sounding data and the variation of these parameters with season is examined. These parameters include the horizontal and vertical wavelength, the ground-based frequency, the eccentricity of the hodograph, the horizontal trace speed,[1] and vertical group velocity.

a. Parameter estimates

Making m the subject in Eq. (3) gives

$$m = \frac{\omega_* - \Omega}{W_b}. \tag{6}$$

[1] Note that the horizontal trace speed is different from the horizontal phase speed, $c_{ph} = \omega K_h/\kappa^2$, where $\kappa^2 = K_h^2 + m^2$.

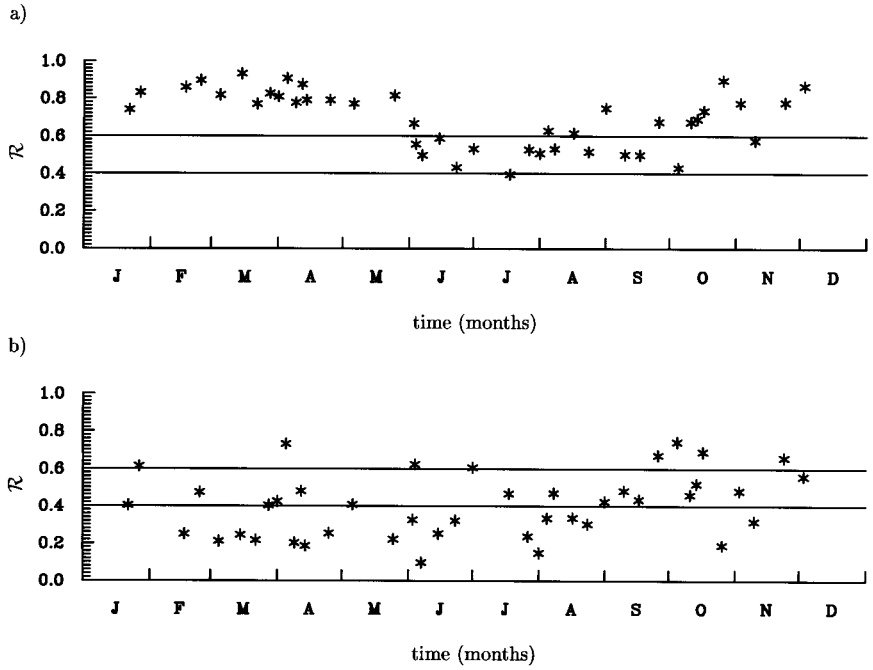

FIG. 5. Time series of the rotary power ratio $\mathcal{R}$ for the 42 flights: (a) above the tropopause and (b) below the tropopause. Values of $\mathcal{R}$ significantly larger than 0.5 (i.e., >0.6, top solid line) indicate a dominance of upward-propagating wave energy and values significantly less than 0.5 (i.e., < 0.4, bottom solid line) indicate a dominance of downward-propagating wave energy.

The three unknowns on the right-hand side of this equation can be calculated from the Omega-sonde soundings. First, the intrinsic frequency ω_* is determined using the Stokes's parameter method. The method is, in essence, a generalization of the hodograph method (see section 3), and a comprehensive description of the technique can be found in Vincent and Fritts (1987) and Eckermann and Vincent (1989). Second, the apparent frequency Ω is taken to be the frequency of the peak in the power spectrum of the perturbation temperature time series. Third, the ascent rate of the balloon, W_b, is calculated directly from the sounding.

Once m is known, the horizontal wavenumber is calculated from the dispersion relation for gravity waves in a rotating atmosphere, that is,

$$K_h^2 = m^2 \frac{(\omega_*^2 - f^2)}{N^2 - \omega_*^2}, \tag{7}$$

where N is the Brunt–Väisälä frequency. Here, the density variation with height has been neglected since $\lambda_z \ll 2\pi H_s$, where H_s is the density scale height. For real m, gravity waves can exist only for intrinsic frequencies in the range $|f| < |\omega_*| < N$. The orientation of the wavenumber vector is determined using the Stokes's parameter method and the temperature variations (see Hamilton 1991). The horizontal trace speed c_{th} and the vertical component of the group velocity, c_{gz}, are given by

$$c_{th} = \frac{\omega}{K_h}, \tag{8}$$

$$c_{gz} = \frac{-(N^2 - f^2)K_h^2}{\omega_* m^3}. \tag{9}$$

Not all soundings are analyzed in this section. We have devised a test to select only those soundings in which the structure of the perturbation wind field is consistent with the assumption that the perturbation is caused by an upward-propagating inertia–gravity wave. The test is, of course, somewhat subjective. Nevertheless, only soundings that satisfy the following criteria are accepted. The first criterion is that $(\overline{u'^2} + \overline{v'^2}) > 8\ \mathrm{m^2\ s^{-2}}$; this ensures that the perturbations are of sufficiently large amplitude. The second criterion is that $\mathcal{R} > 0.6$; this selects only those soundings in which the perturbation wind vector mostly rotates anticyclonically. The 21 soundings that passed this inertia–gravity wave test are marked by asterisks in Fig. 1. The hodographs from almost half of these soundings showed continuous anticyclonic rotation through a depth of more than 10 km.

If we assume that the errors in the observations are independent, then we can use the method outlined by Squires (1968) to estimate the errors in the wave parameters due to the observational errors. In general, if F is a function of A, B, C, with errors ΔA, ΔB, ΔC,

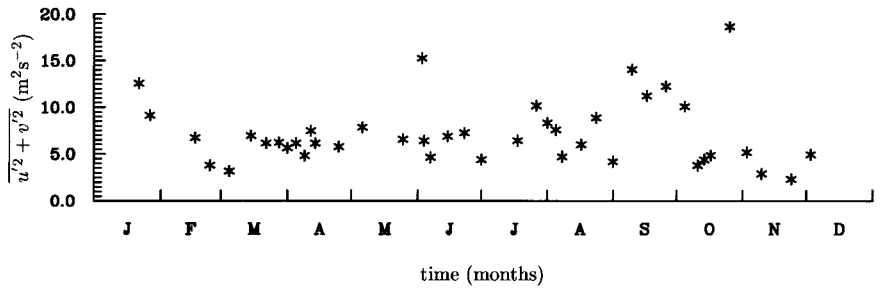

FIG. 6. Time series of the variance of the horizontal perturbation winds, $\overline{u'^2 + v'^2}$.

then the error in F, ΔF, is approximated by the truncated Taylor series

$$(\Delta F)^2 = \left(\frac{\partial F}{\partial A}\right)^2 (\Delta A)^2 + \left(\frac{\partial F}{\partial B}\right)^2 (\Delta B)^2 + \left(\frac{\partial F}{\partial C}\right)^2 (\Delta C)^2. \tag{10}$$

The error in the apparent frequency, Ω, is taken to be $\Delta\Omega$, the resolution of the perturbation temperature power spectrum.

The estimates of the wave parameters calculated from the 21 soundings are shown in Fig. 7 together with the corresponding error estimates. The analyzed vertical wavelengths are between about 1 and 7 km and the horizontal wavelengths lie between 100 and 1000 km. It is difficult to accurately calculate the eccentricity of waves that are nearly circularly polarized, and consequently this leads to large error estimates for the intrinsic frequency. There are three soundings (numbers 12, 18, 21) with very large estimated errors in their horizontal wavelengths because their eccentricities are close to 1.0.

The eccentricities of the waves identified in our analyses lie between 0.5 and 1.0, indicating a relatively high degree of circular polarization. In comparison, Hirota and Niki's (1985) analysis found an eccentricity ($= f/\omega_*$) of about 0.3 with little seasonal variation. However, Eckermann and Hocking (1989) cautioned that eccentricities of around 0.3 could be the result of

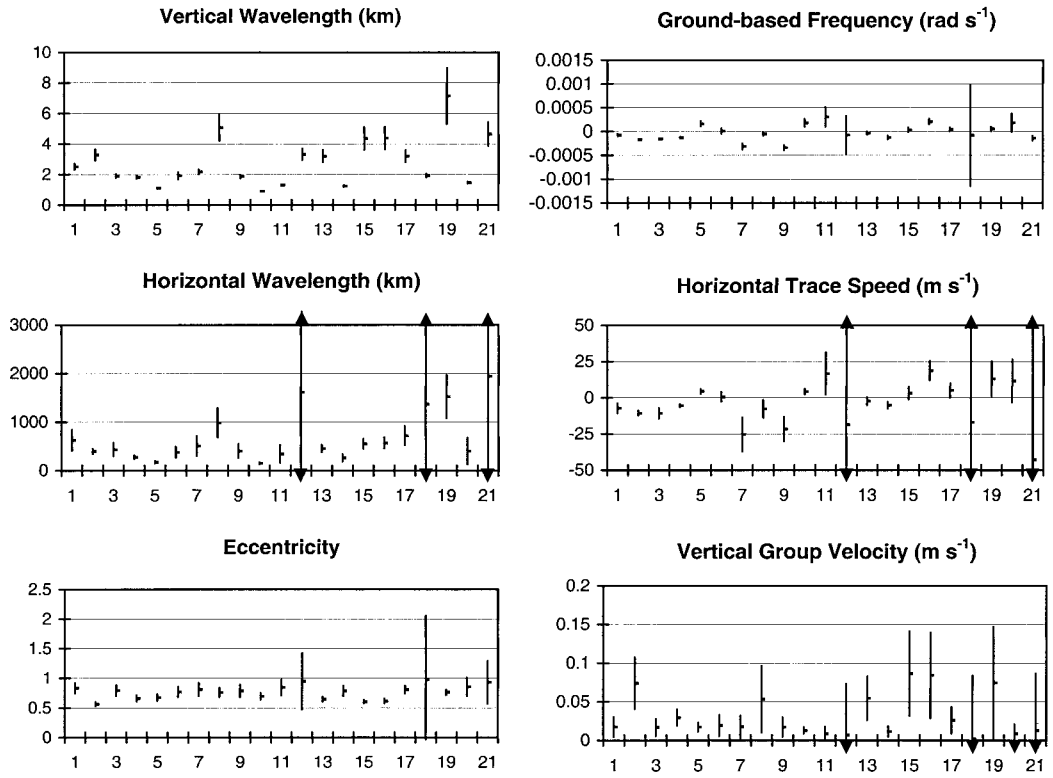

FIG. 7. Time series of vertical and horizontal wavelength, eccentricity, ground-based frequency, horizontal trace speed, and vertical group velocity for the 21 flights that showed clear evidence of inertia–gravity waves. Vertical lines indicate the estimated error for each value. Arrows indicate where the error bars extend beyond the scope of the plot.

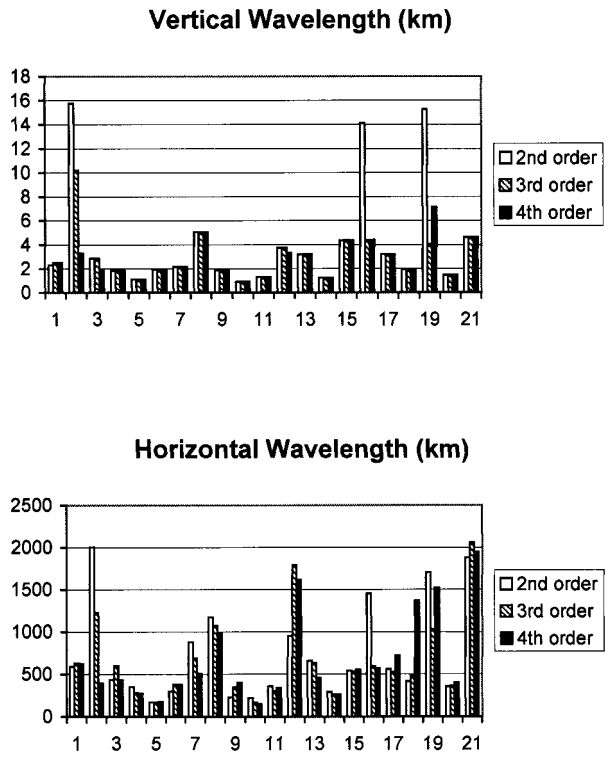

FIG. 8. A comparison of vertical and horizontal wavelengths obtained using second-order (hollow bars), third-order (slant filled bars), and fourth-order polynomials (solid bars) to separate the soundings into background and perturbation profiles for the 21 flights that showed clear evidence of inertia–gravity waves.

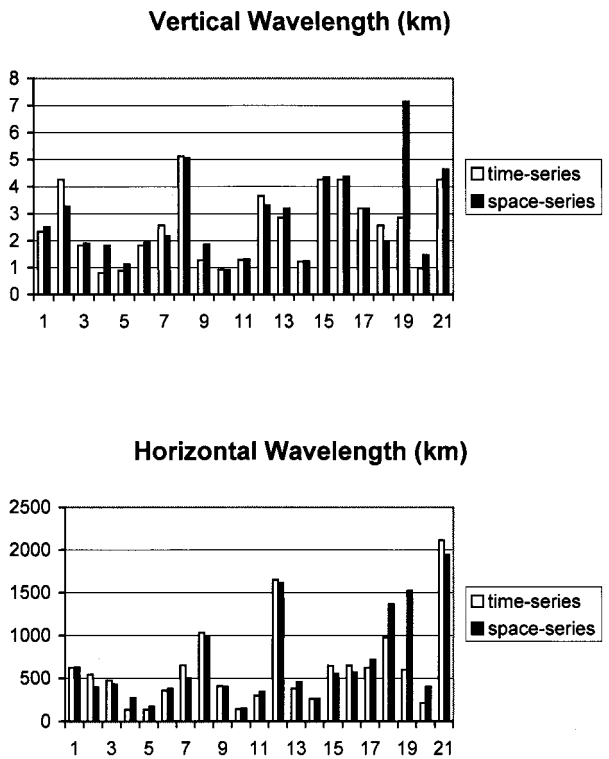

FIG. 9. A comparison of vertical and horizontal wavelengths obtained from treating the soundings as a space series (hollow bars) and a time series (solid bars) for the 21 flights that showed clear evidence of inertia–gravity waves.

a random superposition of small-scale gravity waves for which rotation was unimportant.

Ground-based quantities are obtained by using the background wind (U, V) to Doppler shift their intrinsic counterparts. These calculations use the background wind at 21 km (i.e., the midpoint of the height interval 13.5–28.5 km). The sensitivity of the results to this choice of background wind values will be explored in the next section. The ground-based frequencies are between -4×10^{-4} and 4×10^{-4} rad s^{-1}. Two soundings (numbers 12, 18) have large estimated errors in the ground-based frequency due to large estimated errors in their horizontal wavelengths.

The horizontal trace speed and the vertical group velocity are highly derived quantities and therefore have relatively large errors. The vertical component of the group velocity is small and positive (<0.1 m s^{-1}) consistent with upward-propagating inertia-gravity waves, and the horizontal trace speed is in the range -50 to 30 m s^{-1}.

b. Sensitivity

The errors in the wave parameters discussed in the previous section are based solely on errors in the observations and on how well one can resolve the power

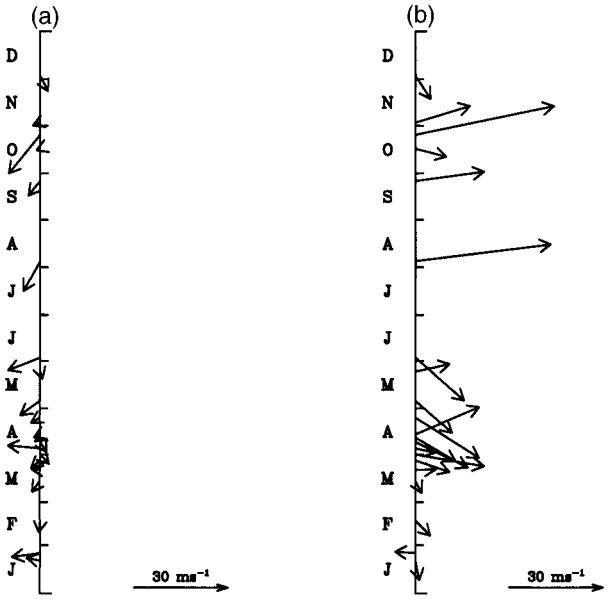

FIG. 10. Time series of horizontal group velocity vectors for the 21 flights showing clear evidence of inertia–gravity waves: (a) intrinsic group velocity and (b) ground-based group velocity. The vectors are oriented with north at the top of the page.

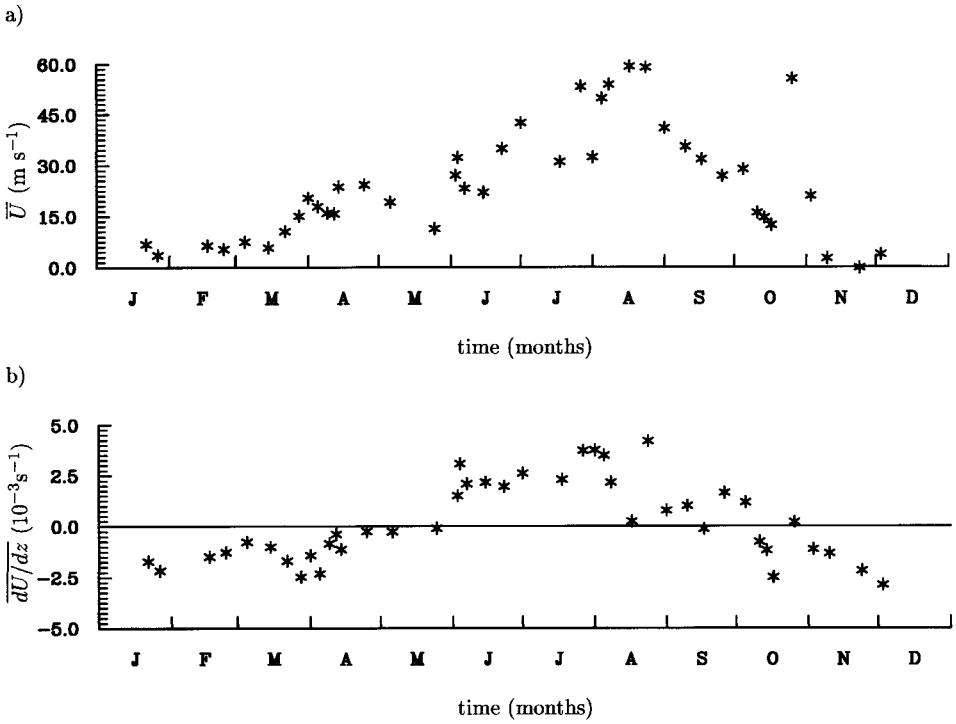

FIG. 11. Time series of (a) the mean background zonal wind $\overline{U}$ and (b) the corresponding vertical shear $\overline{dU/dz}$.

spectrum. We examine now the sensitivity of our results to (a) the choices made in decomposing the sounding into background and perturbation profiles; (b) whether the soundings are treated as time series or instantaneous height series; and (c) the choice of U and V in calculating ground-based quantities.

As discussed in section 2, fourth-order least squares polynomials are used to separate the soundings into background and perturbation profiles. This prompts the question, why not use second-order, third-order, or higher-order polynomials? The analysis height range L is 15 km. Therefore, the maximum vertical wavelength that can be adequately resolved is $L/2 = 7.5$ km, and any perturbations in the flow with vertical wavelengths greater than $L/2$ should be removed (i.e., assigned to the background flow). Roughly speaking, a second-order polynomial removes perturbations with vertical wavelengths greater than $2L$, a third-order polynomial removes perturbations with vertical wavelengths greater than L, and a fourth-order polynomial removes perturbations with vertical wavelengths greater than $2L/3$. Polynomials of order greater than four may remove resolved inertia-gravity wave signals from the perturbation profiles. Thus, we chose fourth-order polynomials in preference to third-order and second-order polynomials, since they remove those perturbations that cannot be adequately resolved. Figure 8 shows a comparison of the horizontal and vertical wavelengths calculated using second-order, third-order, and fourth-order polynomials to represent the background flow. For the most part, the results are not very sensitive to the order of the polynomial fit. However, there are several days on which the second-order polynomial fit seems to predict long vertical wavelengths. This is because the second-order polynomials do not adequately represent slow variations in the background flow and, consequently, these slow variations are interpreted as waves.

One of the features of the analysis presented here is that the soundings are treated as time series, rather than as instantaneous height profiles. As mentioned in section 4a the two methods give similar results when $\gamma \ll 1$ [Eq. (4)]; $\gamma < 0.035$ for all soundings analyzed. Figure 9 compares the vertical and horizontal wavelengths obtained using the two methods for the 21 flights that passed the inertia–gravity wave test. For most flights the wavelengths calculated using the two methods are similar. For example, the difference between the vertical wavelengths using the two methods never exceeds 0.5 km.

Calculations of the ground-based quantities requires an estimate of representative background winds. We have calculated U and V using: 1) background winds averaged over the analysis height range, and 2) background winds at the midpoint of the analysis height range. For 18 of the 21 flights the difference in the ground-based frequency is less than the estimated error.

c. Seasonal variation

Figure 10 shows the time series of the horizontal components of the intrinsic and ground-based group velocities calculated from data in the interval 13.5–28.5 km. In all but one sounding, the horizontal component of the intrinsic group velocity has a northerly (southward) component. The horizontal ground-based group velocity has a pronounced westerly (eastward) component due to the background wind. Time series of the vertically averaged background zonal wind, $\overline{U}$, and its vertical shear $\overline{dU/dz}$ (Fig. 11) show strong seasonal variations. (Here the overbars indicate vertical averaging over the interval from 13.5 to 28.5 km.) During the winter months the background zonal flow is strong and westerly, and the shear is positive. During the warmer months, however, the background zonal flow is much weaker and the shear is negative. Comparing Fig. 11 with Fig. 5a shows that identifiable low-frequency inertia–gravity waves are analyzed in the lower stratosphere most commonly when the background zonal flow is weak and the shear is easterly.

A similar seasonal variation in inertia–gravity wave activity at high latitudes has been reported by Eckermann et al. (1995). These authors found a pronounced minimum in the inertia–gravity activity during winter, with a weaker minimum in summer, and maxima in the inertia–gravity wave activity around the equinoxes. We do not observe the weak summer minimum, but this may be due to insufficient data during the austral summer; we have no soundings during the first half of January and most of December (see Fig. 1).

An important property of inertia–gravity waves is that their hodographs rotate with the intrinsic frequency, and it is this property that is at the heart of most of the analysis methods used so far in this study. The intrinsic frequency can be related to the background flow through the expression $\omega_* = K_h\,|c_{th} - U(z)\cos\varphi|$, where φ is the azimuthal angle between the wind direction and wave-propagation direction. Note that background flow does not affect the intrinsic frequency when it is orthogonal to the direction of wave propagation. From the expression above for ω_* we see that changes in the background wind affect the ellipticity of the wave's hodograph. Eckermann et al. used the above expression for the intrinsic frequency to explain the seasonal variation in inertia–gravity wave activity in their data. For example, if the background zonal wind increases with height, as in winter, the intrinsic frequency increases also. For sufficiently strong westerly shear the waves may become linearly polarized and therefore no longer detectable using methods based on a rotating hodograph. Conversely, the intrinsic frequency will decrease with height during summer since the background westerly flow decreases with height (and becomes easterly). Around the time of the equinoxes, the background zonal wind varies little with height (Fig. 11b) and, consequently, inertia–gravity waves suffer little Doppler shifting to higher (or lower) intrinsic frequencies at this time. Although the Doppler shifting argument outlined above seems to explain the observed seasonal variation in inertia–gravity wave activity, it may only be part of the explanation. For example, there may be a seasonal cycle in the wave generation. We will explore this possibility further in section 6.

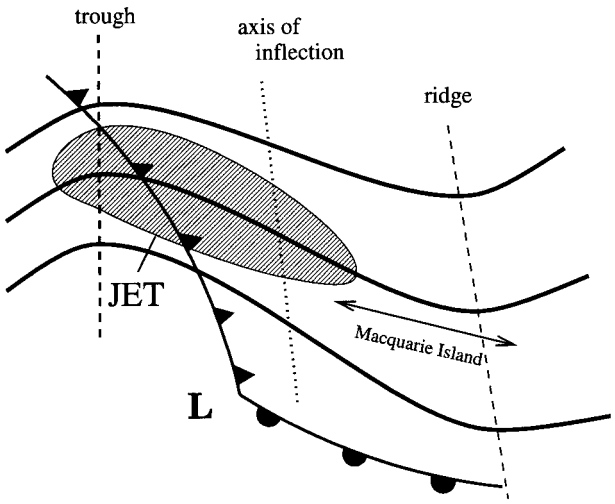

FIG. 12. The 300-hPa height field schematic with Macquarie Island located downstream of the trough roughly between the axis of inflection and the ridge axis. There is a jet–front system in the vicinity of Macquarie Island. The position of a low pressure system is marked by L.

6. Wave sources

We examine now the synoptic conditions under which inertia–gravity waves are generated and propagate over Macquarie Island. Radiosondes released from Macquarie Island are well suited for studying waves generated by sources other than orography since the island is located in the Southern Ocean far from other land masses. The island is essentially a ridge, roughly 32 km long and 4 km wide, and 300 m high. At times, flow over the island generates small-scale gravity waves (e.g., see Mitchell et al. 1990). However, it is unlikely that the waves detected in our analysis are generated by flow over the ridge for two reasons. First, as we will see later, ray-tracing results do not suggest that the island is the source. Second, flow over the ridge would generate stationary waves with a horizontal wavelength on the order of the half-width of the island orography, very different from those shown in Fig. 7.

a. Synoptic pattern

There appears to be a synoptic pattern common to most days on which upward-propagating inertia–gravity waves are analyzed (i.e., pass the inertia–gravity wave test). Figure 12 is a schematic representation of this synoptic pattern. This synoptic pattern is characterized

TABLE 1. Relationship between the location of Macquarie Island and identifiable inertia–gravity waves given in numbers of days.

	Macquarie Island in jet–front vicinity	Macquarie Island *not* in jet–front vicinity
Wave days	16	5
Other days	6	15

by two features: 1) an upper-level jet and associated surface front lying upstream of Macquarie Island; and 2) a 300-hPa height field with Macquarie Island located between the inflection axis[2] and the downstream ridge. This common synoptic pattern is observed on 16 of the 21 days on which inertia–gravity waves were detected. Moreover, the pattern is not observed on 15 of the 21 days on which inertia–gravity waves are not analyzed. These results are summarized in Table 1. There are six days on which the soundings fail the gravity wave test and yet Macquarie Island is in the vicinity of a jet–front system. One of these soundings, 23 February 1994, fails the test because the wave amplitudes are too small (i.e., low variance). Two of the soundings, 3 June 1994 and 16 September 1994, show an anticyclonically rotating hodograph below 19 km (see Fig. 1) but fail the inertia–gravity wave test only because our analysis is confined (for convenience) to the interval between 13.5 and 28.5 km. Uccellini and Koch (1987) reviewed 13 published studies of mesoscale waves over the United States. In every case the observed waves were generated between the inflection axis and the downstream ridge within the exit region of an upper-level jet.

The 0000 UTC National Centers for Environment Prediction (NCEP) reanalyses were examined for each day during 1994, and the monthly frequency with which the common synoptic pattern was analyzed is plotted in Fig. 13. Like the time series of inertia–gravity wave activity (Fig. 5), the frequency of the common synoptic pattern has a minimum during the winter months. This suggests strongly that the seasonal cycle in inertia–gravity wave activity is linked to the seasonal cycle in the large-scale circulation. In particular, there is a minimum in the wintertime because the storm track moves equatorward and the jet–front systems that generate the waves are no longer in a favorable position relative to Macquarie Island.

We consider now how our results compare with previous observational and modeling work on inertia–gravity wave generation and propagation near fronts and upper jets. Reeder and Griffiths (1996) developed a simple two-dimensional numerical model without moist processes in order to investigate the dynamics of developing jet–front systems. They found, among other

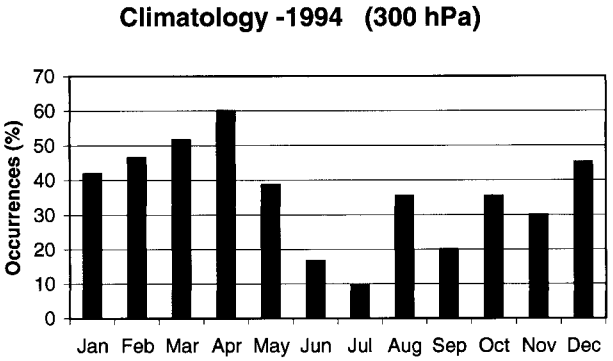

FIG. 13. Climatology of common synoptic pattern, determined from daily 0000 UTC NCEP reanalysis data during 1994.

things, that the rapid evolution of the frontal circulation generates inertia–gravity waves. O'Sullivan and Dunkerton (1995) investigated the generation of inertia–gravity waves in a three-dimensional nonlinear numerical model as a tropospheric jet stream was distorted by a developing baroclinic wave. Inertia–gravity waves arose spontaneously in the regions where parcels experienced strong accelerations, primarily in the jet stream exit region of the upper troposphere. Sato (1994) examined Middle and Upper Atmosphere (MU) radar wind data collected in Shigaraki, Japan (35°N, 136°E), in the three years 1986–88. A strong subtropical westerly jet stream is located over the radar site. Inertia–gravity waves were identified with time series of the variance ($\overline{u'^2 + v'^2}$), and the jet strength showed a similar annual cycle to the wave variance. Table 2 summarizes the results of the present study and compares them with the results of Reeder and Griffiths, O'Sullivan and Dunkerton, Uccellini and Koch, and Sato. The inertia–gravity parameter values calculated here are comparable with those determined in other observational studies and are consistent with theoretical predictions from idealized numerical models.

b. Ray tracing

The source of the inertia–gravity waves observed on 25 October 1994 is investigated now. This day is typical of those on which inertia–gravity waves are analyzed.

The principal tool for identifying possible wave source(s) is GROGRAT, a ray-tracing model developed by Marks and Eckermann (1995). Briefly, the model handles waves of any frequency propagating in a rotating, compressible, and slowly varying atmosphere described by numerically gridded analyses of temperature, horizontal wind, and pressure. These analyses are allowed to evolve with time. Although originally designed for use with coarse, global data in the stratosphere and mesosphere, the model has been reconfigured to use a regional subset of the NCEP reanalyses. These analyses were interpolated onto a grid with resolution 2.5° × 2.5°

[2] An inflection point is where the curve, say, $y = f(x)$, changes concavity from downward to upward or vice versa, that is, $d^2y/dx^2 = 0$.

TABLE 2. Summary of our results and comparison with results presented by others. Our results are those calculated for the 21 flights that passed the gravity wave test. Note that the period column gives results for 20 of the 21 flights. The other flight had a period of 172 h.

Study	Lat.	Long.	Altitude (km)	λ_h (km)	λ_z (km)	f/ω_*	Period (h)
Present study	54°S	159°E	12–30	150–2000	1–7	0.57–0.98	5–55
O'Sullivan and Dunkerton (1995) (day 11)	55°N	23°W	14	600–1000	4	0.63	12–24
Uccellini and Koch (1987) (9 case studies)	31°N	75°W		50–500			1–4
	−49°N	−114°W					
Reeder and Griffiths (1995) at about 18 h			8–10	1000–1064	2.7–2.9	0.77–0.79	10–21
Reeder and Griffiths (1995) at 36 h			22–30	470–500	9.5–12	0.14–0.18	8–14

(20°–80°S, 80°E–180°) in the horizontal and 1 km (0–30 km) in the vertical.

Estimation of the wave parameters from the Omega-sonde flight data within the vertical height range 13.5–28.5 km has been discussed in section 5. For the 25 October 1994 sounding, $k_0 = 2.60 \times 10^{-6}$ m^{-1}, $l_0 = 3.21 \times 10^{-6}$ m^{-1}, $\omega_0 = 5.42 \times 10^{-5}$ rad s^{-1}. In the experiment 125 rays were released using five values for each of k, l, ω:

horizontal wavenumbers:

$$k = k_0 \pm 3 \times 10^{-6}\, n, \qquad n = 0, 1, 2$$

$$l = l_0 \pm 3 \times 10^{-6}\, n$$

ground-based frequencies:

$$\omega = \omega_0 \pm 5 \times 10^{-5}\, n.$$

This defines a cone of rays with a spread in initial values of k, l, ω greater than the errors estimated in section 5a. The rays were released 21 km above Macquarie Island (54.5°S, 158.93°E) and integrated backward in time in order to investigate possible sources. (Note that a height of 21 km was chosen as it is the midpoint of the analysis height interval.)

The rays were divided into groups based on their final location and time. Figure 14 shows typical ray paths projected onto latitude–height cross sections. Wind speed isotachs, corresponding to the time and location of the ray end points are superimposed. This set of rays terminate below an upper-level jet. These rays are projected onto longitude–latitude cross sections and are plotted in Fig. 15. The first panel shows these ray paths from the time of release until they descend to 300 hPa (≈9 km). The contours show geopotential height (solid lines) and wind speed (dashed lines) 27 h after release (roughly the time that the rays reach 300 hPa). The second panel shows the entire ray paths superimposed on horizontal cross sections of pressure (solid contours) and potential temperature (dashed contours) at 3 km, 33 h after release. Together, Figs. 14 and 15 show that the rays move toward the west as they descend through an upper-level jet before terminating 3–4 km above the ground in the vicinity of a cold front. The upper-level jet is downstream of a geopotential height ridge and has an accompanying surface cold front. Other rays, not shown, appeared to terminate in the vicinity of the jet. These features are consistent with the schematic shown in Fig. 12.

7. Summary and conclusions

This study has examined the properties of inertia–gravity waves in the lower stratosphere over Macquarie Island using high-resolution upper-air Omega-sonde soundings launched as part of the 1994 ASHOE–MAE-SA program. The study has also investigated how the properties of the inertia–gravity waves varied with sea-

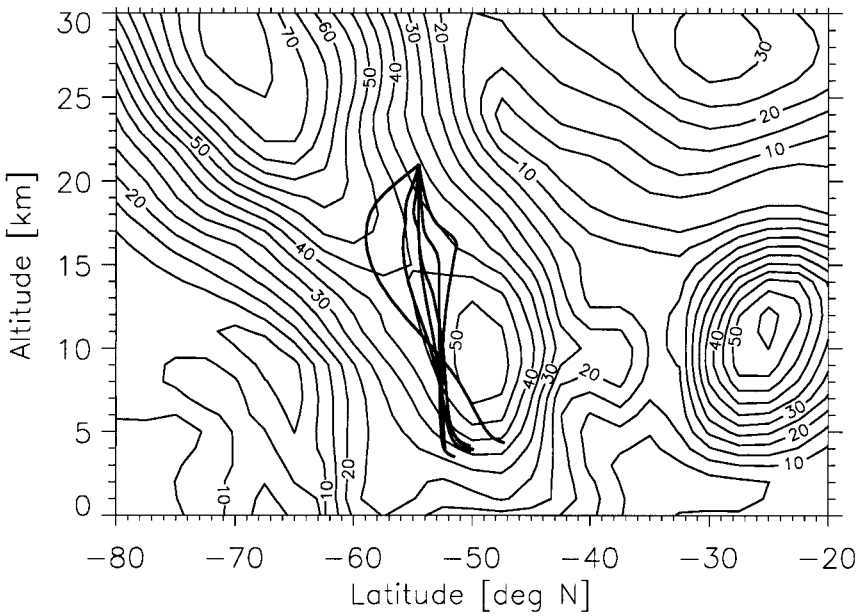

FIG. 14. The projection of typical rays onto latitude–height cross section. Wind speed isotachs 33 h before the ray release time at 95°E are superimposed on the cross section. The end points of the rays shown lie approximately in that plane at the time.

son and the likely source of the waves. Each sounding was partitioned into background and perturbation profiles, and the perturbations were assumed to be gravity waves. The soundings were treated as time series, and the data were analyzed in a frame of reference moving with the radiosonde. It was shown that fourth-order polynomials are well suited to defining the background flow.

Hodograph and rotary spectral analysis showed that anticyclonic rotation (i.e., upward energy propagation) was dominant in the stratosphere, and that cyclonic rotation (i.e., downward energy propagation) was more common in the troposphere. Taken together these results suggested that the source region for the waves was probably in the troposphere. There appeared to be a seasonal cycle in inertia–gravity wave activity above the tropopause with a pronounced reduction in inertia–gravity wave activity during the austral winter. However, the total horizontal variance, which is commonly used as a measure of gravity wave activity, did not show any clear seasonal variation and appeared to bear little relation to results from the hodograph and rotary spectra analyses.

Analysis showed that the inertia–gravity waves have horizontal wavelengths between 100 and 1000 km, vertical wavelengths between about 1 and 7 km, and horizontal trace speeds in the range -50 to 30 m s^{-1}. The vertical component of the group velocity was small and positive ($<$0.1 m s^{-1}), consistent with upward-propagating inertia–gravity waves. The eccentricity of the waves lay between 0.5 and 1.0, indicating a relatively high degree of circular polarization.

The background zonal wind and its vertical shear showed strong seasonal variations. During the winter months the background zonal flow was strong and westerly, and the shear was positive. During the warmer months, however, the background zonal flow is much weaker and the shear is negative. The inertia–gravity wave activity in the lower stratosphere was strongest when the background zonal flow was weak and the shear was easterly. Hence, during the winter months the inertia–gravity waves may suffer Doppler shifting, by the background flow, to higher intrinsic frequencies, rendering them unidentifiable by the methods used herein. This is one possible explanation for the reduced gravity wave activity identified during winter.

Inertia–gravity waves are detected over Macquarie Island on days with a common synoptic pattern. Two features define this synoptic pattern: 1) an upper-level jet and associated surface front lying upstream of Macquarie Island; and 2) a 300-hPa height field with Macquarie Island located between the inflection axis and the downstream ridge. This common synoptic pattern is observed on 16 of the 21 days on which inertia–gravity waves were detected. Moreover, the pattern is not observed on 15 of the 21 days on which inertia–gravity waves are not analyzed. This common synoptic pattern shows a seasonal cycle similar to that found for the inertia–gravity wave activity and appears to be closely connected to the seasonal movement of the storm track.

GROGRAT, the ray-tracing model developed by Marks and Eckermann, was used to search for possible source regions for the identified inertia–gravity waves. A cone of rays was released 21 km above Macquarie Island and traced backward in time. A jet–front system

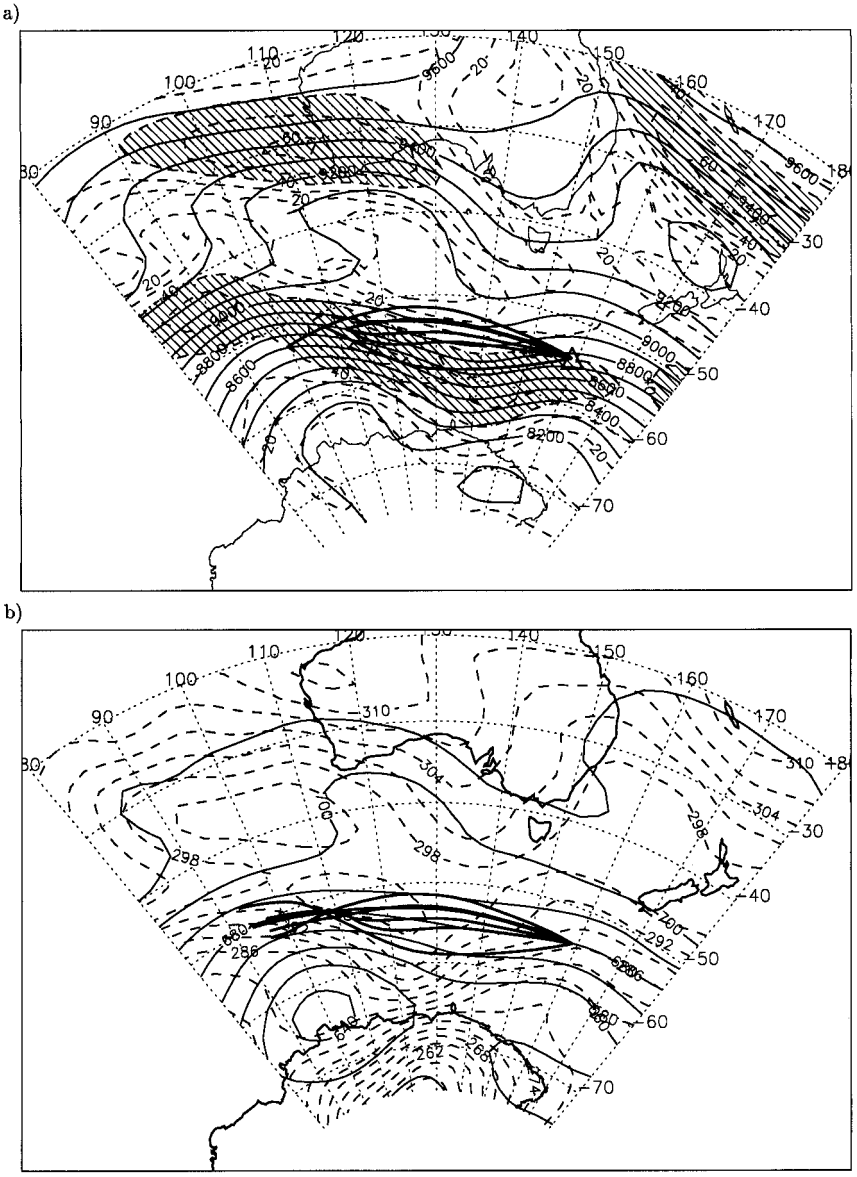

FIG. 15. The projection of typical rays onto longitude–latitude cross sections: (a) ray paths (from the point of release until they descend to 300 hPa) superimposed on cross sections of geopotential height (solid contours) and wind speed (dashed contours); (b) complete ray paths superimposed on cross sections of pressure (solid contours) and potential temperature (dashed contours) at 3 km, 33 h after the rays were released. The end points of the rays shown lie approximately in that plane at that time.

appears to be the source of the inertia–gravity waves. While the ray-tracing has been applied to only one case in this paper, further analysis to be published elsewhere indicates that this case is typical.

Acknowledgments. This work has been partially funded through a dedicated NGAC grant and through support from the Australian Government's Cooperative Research Centres Program. The Omega-sonde data used were kindly provided by Jim Easson and Don Anderson from the Global Atmospheric Watch section of the Australian Bureau of Meteorology.

REFERENCES

Allen, S. J., and R. A. Vincent, 1995: Gravity-wave activity in the lower atmosphere: Seasonal and latitudinal variations. *J. Geophys. Res.,* **100,** 1327–1350.

Bacmeister, J. T., S. D. Eckermann, P. A. Newman, L. Lait, K. R. Chan, M. Loewenstein, M. H. Proffitt, and B. L. Gary, 1996: Stratospheric horizontal wavenumber spectra of winds, potential

temperature, and atmospheric tracers observed by high-altitude aircraft. *J. Geophys. Res.,* **101,** 9441–9470.

Barat, J., and C. Cot, 1992: Wind shear rotary spectra in the atmosphere. *Geophys. Res. Lett.,* **19,** 103–106.

Eckermann, S. D., and W. K. Hocking, 1989: Effect of superposition on measurements of atmospheric gravity waves: A cautionary note and some reinterpretations. *J. Geophys. Res.,* **94,** 6333–6339.

——, and R. A. Vincent, 1989: Falling sphere observations of anisotropic gravity wave motions in the upper stratosphere over Australia. *Pure Appl. Geophys.,* **130,** 509–532.

——, I. Hirota, and W. K. Hocking, 1995: Gravity wave and equatorial wave morphology of the stratosphere derived from long-term rocket soundings. *Quart. J. Roy. Meteor. Soc.,* **121,** 149–186.

Fritts, D. C., 1993: Gravity wave sources, source variability and lower and middle atmosphere effects. *Coupling Processes in the Lower and Middle Atmosphere,* E. V. Thrane, T. A. Blix, and D. C. Fritts, Eds., Kluwer Academic, 191–208.

Gill, A. E., 1982: *Atmosphere–Ocean Dynamics.* Academic Press, 622 pp.

Gonella, J., 1972: A rotary-component method for analysing meteorological and oceanographic vector time series. *Deep-Sea Res.,* **19,** 833–846.

Hamilton, K., 1991: Climatological statistics of stratospheric inertia-gravity waves deduced from historical rocketsonde wind and temperature data. *J. Geophys. Res.,* **96,** 20 831–20 839.

Hirota, I., and T. Niki, 1985: A statistical study of inertia-gravity waves in the middle atmosphere. *J. Meteor. Soc. Japan,* **63,** 1055–1065.

Karoly, D. J., G. L. Roff, and M. J. Reeder, 1996: Gravity wave activity associated with tropical convection detected in TOGA COARE sounding data. *Geophys. Res. Lett.,* **23,** 261–264.

Leaman, K. D., and T. B. Sanford, 1975: Vertical energy propagation of inertial waves: A vector spectral analysis of velocity profiles. *J. Geophys. Res.,* **80,** 1975–1978.

Marks, C. J., and S. D. Eckermann, 1995: A three-dimensional nonhydrostatic ray-tracing model for gravity waves: Formulation and preliminary results for the middle atmosphere. *J. Atmos. Sci.,* **52,** 1959–1984.

Mitchell, R. M., R. P. Cechet, P. J. Turner, and C. C. Elsum, 1990: Observation and interpretation of wave clouds over Macquarie Island. *Quart. J. Roy. Meteor. Soc.,* **116,** 741–752.

Reeder, M. J., and M. Griffiths, 1996: Stratospheric inertia-gravity waves generated in a numerical model of frontogenesis. II: Wave sources, generation mechanisms and momentum fluxes. *Quart. J. Roy. Meteor. Soc.,* **122,** 1175–1195.

O'Sullivan, D., and T. J. Dunkerton, 1995: Generation of inertia-gravity waves in a simulated life cycle of baroclinic instability. *J. Atmos. Sci.,* **52,** 3695–3716.

Sato, K., 1994: A statistical study of the structure, saturation and sources of inertio-gravity waves in the lower stratosphere observed with MU radar. *J. Atmos. Terr. Phys.,* **56,** 755–774.

Squires, G. L., 1968: *Practical Physics.* McGraw-Hill, 224 pp.

Tsuda, T., Y. Murayama, H. Wiryosumarto, S. B. Harijono, and S. Kato, 1994: Radiosonde observations of equatorial atmosphere dynamics over Indonesia. Part 2. Characteristics of gravity waves. *J. Geophys. Res.,* **99,** 10 507–10 516.

Uccellini, L. W., and S. E. Koch, 1987: The synoptic setting and possible energy sources for mesoscale wave disturbances. *Mon. Wea. Rev.,* **115,** 721–729.

Vincent, R. A., 1984: Gravity-wave motions in the mesosphere. *J. Atmos. Terr. Phys.,* **46,** 119–128.

——, and D. C. Fritts, 1987: A climatology of gravity wave motions in the mesopause region at Adelaide, Australia. *J. Atmos. Sci.,* **44,** 748–760.

——, S. J. Allen, and S. D. Eckermann, 1997: Gravity wave parameters in the lower stratosphere. *Gravity Wave Processes: Their Parameterization in Global Climate Models,* K. Hamilton, Ed., Springer-Verlag, 7–25.